Surface & Coatings Technology 416 (2021) 127162

Contents lists available at ScienceDirect

Surface & Coatings Technology

journal homepage: www.elsevier.com/locate/surfcoat

Improving phase stability, hardness, and oxidation resistance of reactively magnetron sputtered (Al,Cr,Nb,Ta,Ti)N thin films by Si-alloying

Andreas Kretschmer [a,*], Alexander Kirnbauer [a], Vincent Moraes [a], Daniel Primetzhofer [b], Kumar Yalamanchili [c], Helmut Rudigier [c,d], Paul Heinz Mayrhofer [a]

[a] *Institute of Materials Science and Technology, TU Wien, Getreidemarkt 9, 1060 Vienna, Austria*
[b] *Department of Physics and Astronomy, Uppsala University, SE-75120 Uppsala, Sweden*
[c] *Oerlikon Balzers, Oerlikon Surface Solutions AG, Iramalli 18, 9496 Balzers, Liechtenstein*
[d] *OC Oerlikon Management AG, 8808 Pfäffikon, SZ, Switzerland*

ARTICLE INFO

Keywords:
High-entropy metal-sublattice nitrides (HESN)
High-entropy alloys (HEA)
Oxidation
Thermal stability
Magnetron sputtering
PVD

ABSTRACT

Reactively magnetron sputtered high-entropy metal-sublattice (Al,Cr,Nb,Ta,Ti)N coatings have been alloyed with Si concentrations between $x_{Si} = 6.4$ and 15.0 at.%. All coatings are single-phase fcc structured and their hardness initially increases from ~32 to 35 GPa with Si-alloying up to $x_{Si} = 9.8$ at.%, and then decreases to ~24 GPa for higher Si contents. Contrary, the indentation modulus E continuously decreases from ~470 to 350 GPa by Si-alloying. Also, the decomposition of the fcc structure during vacuum annealing is shifted from 1000 to 1200 °C with the addition of Si. The hardness initially increases during vacuum annealing and reaches a maximum of 37 GPa with $T_a = 1000$ °C at $x_{Si} = 12.0$ at.%. During oxidation experiments in ambient air at 850 °C for up to 100 h, a 2700 nm single-phase rutile-structured oxide scale forms at the Si-free (Al,Cr,Nb,Ta,Ti)N with a parabolic growth rate. The rate changes to a logarithmic-like behavior with the addition of Si, resulting in only ~280 nm oxide scale after 100 h. Also, for the Si-containing coatings, the oxide scale shows only one crystalline rutile structure. The pore size in the oxide scale of the Si-free coating is considerably reduced by Si-addition. The oxides growing at the Si-containing coatings show an opposing Si- and Cr-gradient - with much smaller pores in the Si-rich inner region - which shows a gradual transition to the remaining nitride. Ab initio based calculations confirm that the formation of a single-phase rutile-structured solid solution oxide, $(Al,Cr,Nb,Ta,Ti)O_2$, is energetically preferred over separate phases above 509 K, due to the higher configurational entropy. Below this temperature the decomposition towards $(Al,Ta,Ti)O_2$ + $(Cr,Nb)O_2$ would be favored (when considering just chemical contributions), but kinetically restricted.

1. Introduction

A common strategy to increase the lifetime of machining tools, which need to resist wear under harsh conditions, is the use of hard protective coatings. TiN, (Ti,Al)N, (Al,Cr)N, and similar nitride based materials have been developed to protect various machining tools from abrasion and oxidation [1–7]. Especially when synthesized by chemical or physical or vapor deposition (PVD) - allowing for extended solubility limits - the addition of selected alloying elements is a powerful approach to further improve their desired properties.

In 2004, Cantor et al. [8] and Yeh et al. [9] developed so-called high-entropy alloys (HEA), which consist of five or more principal elements with an equiatomic or near-equiatomic composition. Hence, this compound contains no dominant species. High-entropy materials are commonly characterized by four core effects: high configurational entropy $\Delta S_{config} > 1.5 \cdot R$ (R being the universal gas constant), a highly distorted crystal lattice, sluggish diffusion and the cocktail-effect [10–12]. This concept has also been expanded to high-entropy ceramics, which after a simplified notation [13,14] consist of at least five constituting binaries. A more-precise and accurate notification was introduced recently [15] with high-entropy sublattice (HES) ceramics. As in principle only the metal-sublattice has a high entropy [14],

---

* Corresponding author.
E-mail addresses: Andreas.Kretschmer@tuwien.ac.at (A. Kretschmer), Alexander.Kirnbauer@tuwien.ac.at (A. Kirnbauer), Vincent.Moraes@tuwien.ac.at (V. Moraes), daniel.primetzhofer@physics.uu.se (D. Primetzhofer), Kumar.Yalamanchili@oerlikon.com (K. Yalamanchili), Helmut.Rudigier@oerlikon.com (H. Rudigier), Paul.Mayrhofer@tuwien.ac.at (P.H. Mayrhofer).

https://doi.org/10.1016/j.surfcoat.2021.127162
Received 9 February 2021; Received in revised form 5 April 2021; Accepted 6 April 2021
Available online 16 April 2021
0257-8972/© 2021 The Author(s). Published by Elsevier B.V. This is an open access article under the CC BY license (http://creativecommons.org/licenses/by/4.0/).

whereas the non-metal-sublattice is formed basically by one principal element, when combining various nitrides [15–18], carbides [19–21], oxides [22,23], borides [14,24–26], or silicides [27,28]. Thereby, the respective non-metal occupies its own sublattice, whereas the different metal species are randomly distributed on their sublattice. Consequently, the configurational entropy essentially stems from the metal sublattice, if the non-metal sublattice is occupied by one element. By the common definition, $\Delta S_{config} > 1.5 \cdot R$, such a material would not be considered high-entropic, but this value was intended for metallic alloys.

Ceramics are an entirely different material class, therefore when searching for the high-entropy effect in a ceramic, this criterion should be adjusted accordingly. A high-entropy material is characterized by the lack of a dominant solvent in a solid solution with many elements. For five or more components in near-equiatomic composition, such an arrangement, which is always accompanied by a high configurational entropy compared to conventional alloys, leads to a highly distorted lattice and other favorable properties of high-entropy materials. Additionally, the positions of the non-metal atoms are not independent from the metal sublattice. On the contrary, each non-metal atom is bound to a strongly varying surrounding, similar to each metal atom in an alloy. Therefore, we alter the definition of a high-entropy ceramic so that the configurational entropy is not considered per atom, but per constituting binary compound [14]. This approach is convenient, since the numerical value for classifying a high-entropy material then matches the criterion for metallic alloys ($\Delta S_{config} > 1.5 \cdot R$) for all kinds of stoichiometric ratios in ceramics.

The high-entropy effects lead to materials that possess excellent mechanical properties and are stable at high temperatures [17,18,29,30]. Furthermore, the transport of ionic or atomic species through the lattice is significantly retarded [31–34]. These key-properties advocate this material class as suitable candidates for protective coatings. However, most studies on high-entropy sublattice nitrides (HESN) have been performed in vacuum conditions, whereas in real-life applications the presence of O_2 is limiting the durability of these materials. Many studies have been performed to tailor oxidation resistance in low-entropy nitrides, by adding Ta, Y, or Ce for example [5,35–37]. We still lack such studies for high-entropy ceramics. To our knowledge, the most notable work on this problem was done by Shen et al. by developing the high-entropy nitride $(Al_{0.34}Cr_{0.22}Nb_{0.11}Si_{0.11}Ti^{0.22})_{50}N_{50}$ with exceptional oxidation resistance at high temperatures [16]. They attribute this property to the presence of dense layers of Al_2O_3 and amorphous oxide layers, which are largely composed of Si-oxides. In this work we present the impact of Si-alloying on the similar material system (Al,Cr,Nb,Ta,Ti)N and the resulting improvements to not only oxidation resistance, but also phase stability and mechanical properties.

2. Experimental details

2.1. Deposition process

We used reactive magnetron sputtering with a modified Leybold Heraeus Z400 magnetron sputtering system, equipped with a powder metallurgically prepared 75-mm-diameter target of equimolar Al, Cr, Nb, Ta, and Ti composition (Plansee Composite Materials GmbH). Si was added by placing 8, 12, 16, or 24 ($2 \times 2 \times 0.38\ mm^3$) pieces evenly on the cathode racetrack. The $Al_uCr_vNb_wTa_xTi_ySi_zN$ coatings were deposited on (1 0 0)-oriented Si ($20 \times 7 \times 0.38\ mm^3$) and ($1\ \bar{1}\ 0\ 2$) sapphire ($10 \times 10 \times 0.53\ mm^3$) substrates, mounted face-to-face to the target at a distance of 4 cm. For all depositions the base pressure was below 0.3 mPa, the deposition temperature was 440 °C and the bias potential was −50 V DC. Before the deposition process, the substrates were Ar-ion etched at a pressure of 1.3 Pa for 15 min by applying a pulsed DC substrate potential of −150 V, the pulse frequency was 150 kHz and the pulse duration 2496 ns.

The target was also cleaned by sputtering for 2 min behind the closed shutter. A 18 sccm/22 sccm gas mixture of N_2 and Ar (both 99.999% purity) at a pressure of 0.43 mbar was used for the deposition. The cathode was operated with a constant current of 1.0 A (power density of 11.9 W/cm^2) and 0.75A (power density of 9.1 W/cm^2) without and with Si pieces on the racetrack, respectively, for 20 min in all cases. The reduction of the sputtering-current for preparing the Si-alloyed coatings was needed to prevent breaking of the Si substrates due to increased growth stresses.

2.2. Sample analysis

Cross-sections of the coatings on Si-substrates were analyzed with a FEI Quanta F200 scanning electron microscope (SEM) - equipped with a field emission gun (FEG) and operated at 5 kV - to investigate growth morphology and deposition rates. Chemical compositions of as-deposited coatings were analyzed by time-of-flight elastic recoil detection analysis (ToF-ERDA) with a recoil detection angle of 45° using a beam of 36 MeV I^{8+} ions. Experimental details, data analysis, as well as potential systematic uncertainties are described elsewhere [38–40]. The crystal structure was investigated with X-ray-diffraction (XRD) using a PANanlytical XPert Pro MPD ($\theta - \theta$ diffractometer) equipped with a Cu-Kα source ($\lambda = 0.15408\,nm$, 45 kV and 40 mA) in Bragg-Brentano geometry. Samples on sapphire substrates were vacuum annealed in a Centorr LF22-2000 vacuum furnace at $T_a = 800$, 900, 1000, 1100, and 1200, the heating rate was 20 K/min, the holding time 10 min, and the passive (simply turning off the heater) cooling rate at least 50 K/min down to 200 °C.

To study the oxidation resistance of the coatings, the thickness as well as chemistry of the oxide scale growing at 850 °C were studied by SEM. After an oxidation treatment within an ambient-air furnace at 850 °C for 0.5, 1, 5, 10, 30, and 100 h, the coated sapphire samples were extracted from the hot zone, cooled down to room temperature, and prepared for cross-sectional investigations. The mirror polished embedded cross sections were analyzed by energy dispersive X-ray spectroscopy-linescans (EDS) across the oxide scale using a 20 kV electron beam. Transmission electron microscopy (TEM) was performed with a FEI TECNAI F20, equipped with a FEG, operated at 200 kV, on as-deposited and oxidized samples.

Mechanical properties were determined using an ultra-micro-indentation system (UMIS) equipped with a Berkovich tip. Indentation hardness, H, and modulus, E, – which, depending on materials behavior during indentation, may also be treated as Young's modulus – were obtained by evaluating the unloading segments of the indentation curves after Oliver and Pharr [41] assuming a Poisson's ratio of 0.25.

2.3. DFT calculations

DFT calculations were carried out with the Vienna ab initio simulation package (VASP) [42,43], using projector augmented plane wave (PAW) pseudo-potentials under the generalized gradient approximation [44] to study the solid solution of $(Al,Cr,Nb,Ta,Ti)O_2$ in rutile structure, with equimolar composition, and possible decomposition products. A plane-wave cut-off energy of 600 eV, and a Γ-centered Monkhorst-Pack k-mesh [45] with $6 \times 6 \times 7$ points were used. The accuracy was set to 10^{-5} eV/atom. The cells were relaxed regarding volume, shape and atomic positions. The decomposition of equiatomic $(Al,Cr,Nb,Ta,Ti)O_2$ into all possible combinations of lower-order oxides (binary, ternary, quaternary, and quintenary oxides) with equimolar composition was considered. All oxides were rutile structured (space group 136 $P4_2/mnm$), with the exception of the binaries, which were calculated both in rutile structure and their common stable structures. These are Al_2O_3 (α-structure, space group 167 $R-3c$), Cr_2O_3 (Al_2O_3-prototype, space group 167 $R-3c$), Nb_2O_5 (space group 10 $P12/m1$), Ta_2O_5 (space group 25, $Pmm2$), and TiO_2 in rutile structure. The binaries were calculated from single cells, while all multinary oxides were calculated from a 3 × 3 × 2 supercell with 72 atoms in total. The metals were placed on their sublattice with the special quasi-random structure (SQS) method [46]. To reach equiatomic composition for the hexinary oxide (25 atoms on 24 positions), five permutations with different occupations, leaving one atom per metallic species out in turn, were calculated and averaged.

The thermodynamic phase stability is determined by the free enthalpy of mixing

$$\Delta G_{mix} = \Delta H_{mix} - T\Delta S_{mix} \tag{1}$$

where ΔH_{mix} is

$$\Delta H_{mix} = E_f^{Educt} - \sum_i \nu^i E_f^i \tag{2}$$

T is the absolute temperature, ΔS_{mix} the mixing entropy, calculated from the difference of configurational entropies S_{config} between educt and product phases, E_f is the energy of formation, and ν^i the stoichiometric coefficient of component i. Since the mixing entropy is contained in the metal sublattice, and E_f is usually given in eV/atom, the mixing entropy needs to be related to the formula unit. When using the formula [9]

$$S_{config} = -R\sum_i X_i lnX_i \tag{3}$$

to calculate the configurational entropy, the entropy has to be divided by 3 to get the correct value in eV/atom for the MO_2 stoichiometry.

3. Results and discussion

3.1. Chemical composition and growth morphology

The results of the chemical analysis with ERDA are shown in Table 1. The depth profiles were all homogenous except for a thin surface oxide layer, the concentrations were therefore calculated from the bulk signals of the coatings. All coatings are over-stoichiometric with a N-content of >5.49 at.%. Since the masses of Al and Si could not be distinguished, only a sum of both elements is available. However, by calculating the average elemental ratio of Al to the other metals in the Si-free sample, the Al content and thus the Si content can be estimated for the other samples. With increasing number of Si-pieces on the racetrack the concentrations of the other metals decrease, but not proportionally to each other. In the coating with the highest Si-content the Cr, Nb, Ta, and Ti concentrations decrease by 34, 33, 39, and 38%, respectively, compared to the Si-free sample. The average decrease of up to 36% (in the coating with the highest Si concentration) was used to estimate the Al concentration, the Si concentration was then calculated as difference to the sum signal.

Table 1
Chemical analysis in at.% as deduced from ToF-ERDA. Since the masses of Al and Si could not be distinguished, their ratio is estimated from the Al ratio to the other metals in the sample without Si. The given uncertainties are the statistical standard errors, for Al and Si in Si-containing coatings the standard error of the sum concentration is given. ΔS_{config} of the metal sublattice is given as multitude of R and is always $\geq 1.52 \cdot R$.

Si-pieces	Al	Cr	Nb	Si	Ta	Ti	N	$\Delta S_{config} \cdot R$
0	9.6 ± 0.1	11.6 ± 0.1	7.0 ± 0.1	0.0	7.1 ± 0.2	9.4 ± 0.1	55.4 ± 0.4	1.52
8	8.1 ± 0.1	10.9 ± 0.1	6.2 ± 0.1	6.4 ± 0.1	5.4 ± 0.1	7.7 ± 0.2	54.9 ± 0.3	1.68
12	7.3 ± 0.3	9.1 ± 0.1	5.8 ± 0.1	9.8 ± 0.3	4.9 ± 0.1	6.9 ± 0.1	55.4 ± 0.2	1.66
16	6.8 ± 0.1	7.5 ± 0.1	5.4 ± 0.1	12.0 ± 0.1	5.0 ± 0.1	6.6 ± 0.1	55.9 ± 0.2	1.63
24	6.1 ± 0.2	7.7 ± 0.1	4.7 ± 0.1	15.0 ± 0.2	4.4 ± 0.1	5.8 ± 0.1	55.0 ± 0.3	1.59

Contrary to the metals, the N-content stays in a range between 54.9 and 55.9 at.%. This over-stoichiometry could be supported by metal vacancies, as was shown for TaN with ab-initio calculations [47], and the slightly different stoichiometry of Si_3N_4. All stated uncertainties are standard errors, for Al and Si in Si-containing coatings the standard error of the sum concentration is given. The configurational entropy S_{config} is highest in the sample with 9.8 at.% Si, and always $\geq 1.52 \cdot R$ (considered per formula unit). Therefore, by our definition all coatings can be considered HESN.

In Fig. 1, the SEM-micrographs of the fracture cross-sections of as-deposited coatings reveal dense microstructures and smooth surfaces. Nevertheless, the addition of Si clearly influences the growth morphology of the individual coatings starting from a relatively coarse grained and columnar structure for the Si-free sample (Fig. 1a). Increasing the Si content to 6.4 to 9.8 to 12.0 at.% results in a less-pronounced columnar growth structure, Fig. 1b, c, and d, respectively, and even an almost featureless structure for the 15.0at Si-containing coating (Fig. 1e). The deposition rates are 160 nm/min without Si at 1.0A target current, and between 85 and 140 nm/min with Si at 0.75A target current. The total coating thicknesses in order of increasing Si contents are 3.2, 2.0, 1.7, 2.3, and 2.7 μm, respectively. When the latter deposition rates are normalized to a current of 1A, the growth rates lie between 113 and 186 nm/min. Thus, the differences in growth rates basically stem from the Si platelets added to the racetrack and the individual elements.

TEM analysis of our coatings on sapphire substrates support the growth morphology results obtained by SEM. Exemplarily, we show cross-sectional TEM images for the (Al,Cr,Nb,Ta,Ti)N coating without Si and with 9.8 at.% Si in Fig. 2a and b, respectively. Although the mean column diameter decreases by the addition of 9.8 at.% Si, their columnar structure is still clearly present. The corresponding selected area electron diffraction patterns (taken at positions marked by I and II in Fig. 2a and b, respectively) yield single-phase solid solutions with rock-salt structure (B1, NaCl-prototype, face centered cubic, fcc). The more ring-like SAED pattern for the Si-free sample hints towards a more random growth orientation. The 9.8 at.% Si alloyed (Al,Cr,Nb,Ta,Ti)N coating shows more individual SAED spots suggesting a highly oriented growth. This is also because the individual columns seem to be longer for the 9.8 at.% Si-containing coating. Therefore, the selected area for the SAED pattern covers basically only one column length for the 9.8 at.% Si-containing coating but several ones for the Si-free HESN, see Fig. 2b and a, respectively. Dark field investigations nicely show that the Si-free coating (Fig. 2c) has shorter columns than the 9.8 at.% Si-containing one (Fig. 2d). Interestingly, as suggested already by the bright field investigations, the mean column diameter decreases from around 50 to 25 nm with increasing Si content.

Spatially resolved analysis of the Si concentration is problematic due to the coincidence of the Si and Ta signals in the EDS spectrum, as well as the partial overlap of Si and Al and Si and Ta edges in the electron energy loss spectrum (EELS). But in a plan-view TEM sample of the HESN with 9.8 at.% Si we could find an indication that Si is enriched in the grain boundary region, similar to TiN when alloyed with more than 4 at.% Si [48,49]. The corresponding plan-view bright field and dark field images in Fig. 3a and b show that the column diameters agree well with those obtained from the cross-sectional investigations presented in Fig. 2d. In scanning transmission electron microscopy (STEM) mode with a high angle annular dark field (HAADF) detector the contrast is generated by local sample mass and thickness. Since this sample was prepared by focused ion beam we can exclude high thickness differences to cause local intensity variations. The bright spot in Fig. 3c can therefore be assigned to a grain with either higher atomic mass or to closer alignment

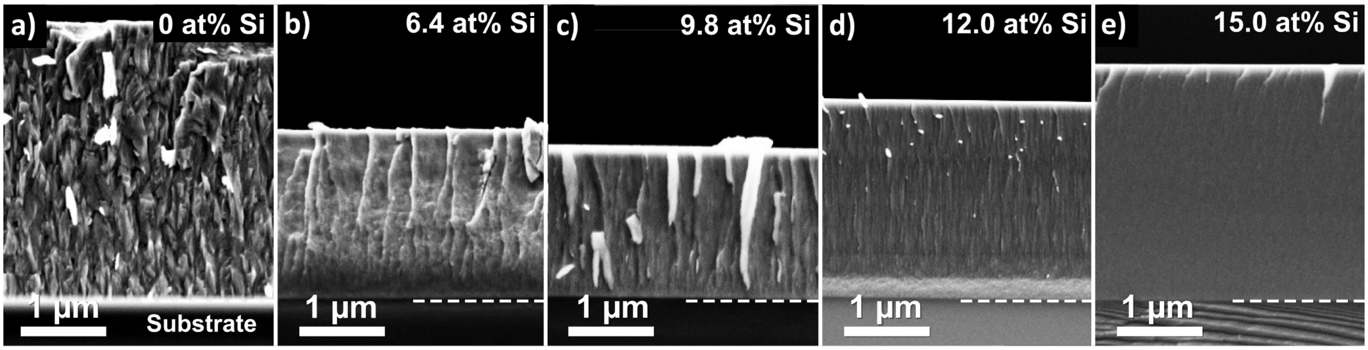

Fig. 1. SEM fracture cross-sections of as-deposited (Al,Cr,Nb,Si,Ta,Ti)N coatings with 0 at.% Si (a), 6.4 at.% Si (b), 9.8 at.% Si (c), 12.0 at.% Si (d), and 15.0 at.% Si (e), deposited on (100) Si substrates. The columnar structure becomes finer with increasing Si-content, and the coating with 15.0 at.% Si even shows a feature-less growth morphology.

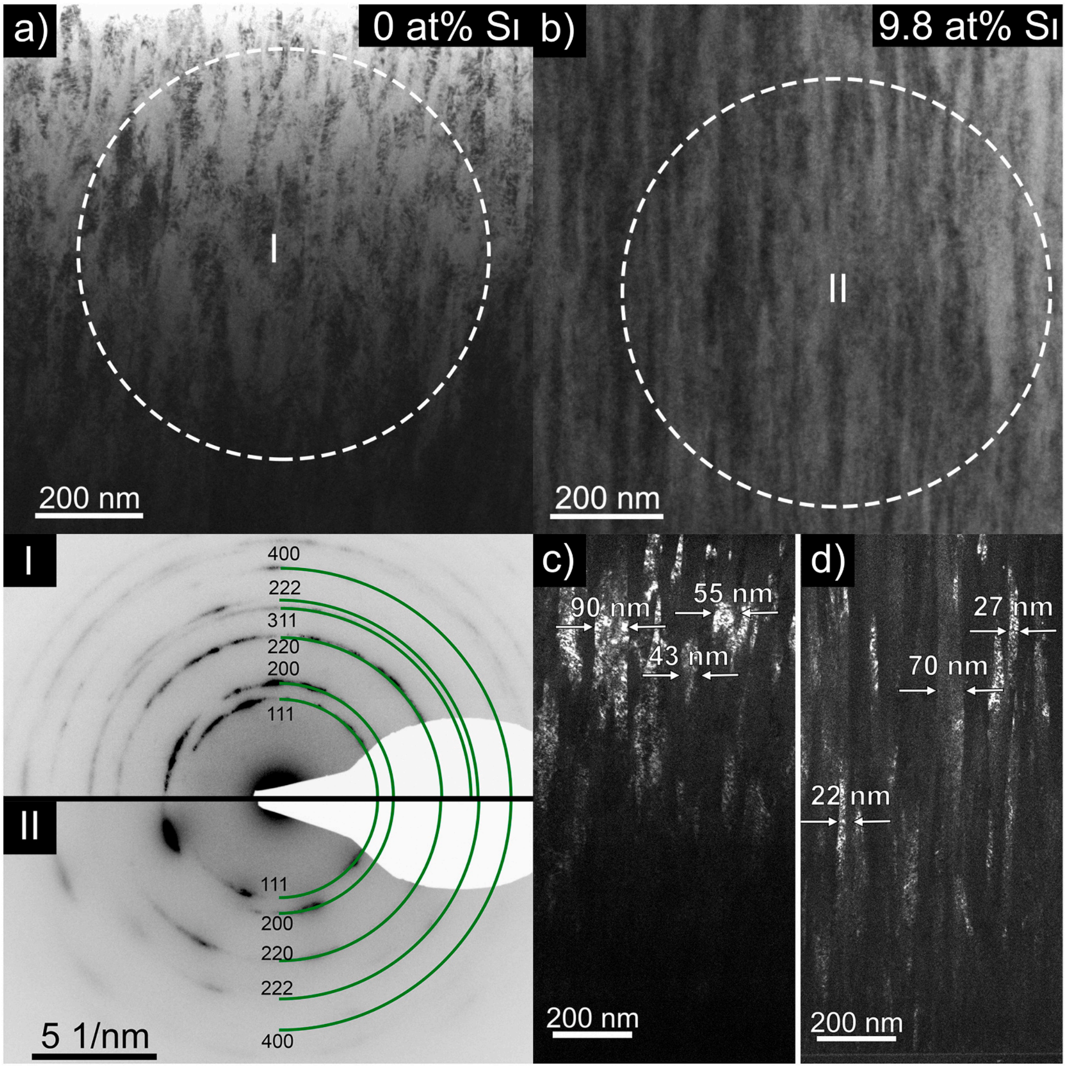

Fig. 2. Bright field cross-sectional TEM-images of the HESN coating without Si (a), and with 9.8 at.% Si (b). The SAED patterns taken from the region I (Si-free sample) and II (9.8 at.% Si-containing sample) show single-phase solid solutions with rock-salt structure for both coatings. Dark field images of the coatings without Si (c) and with 9.8 at.% Si (d), show that Si alloying causes thinner but longer columns.

to a zone axis than its surrounding. An EELS linescan across this grain reveals a decreased Si/Al ratio in the center of the grain and an increased Si/Al ratio at the grain boundaries. Since Al is expected to be accompanying the other metals, this linescan supports the mass contrast in the STEM-HAADF image. In high-resolution mode, Fig. 3d, the triple-junction between three crystalline grains reveals a region with perturbed lattice planes. This could be an amorphous grain-boundary region, but careful interpretation is necessary since such a feature can also be generated by the projection of two overlapping grains.

A fast Fourier transformation (FFT) of the blue margined area in

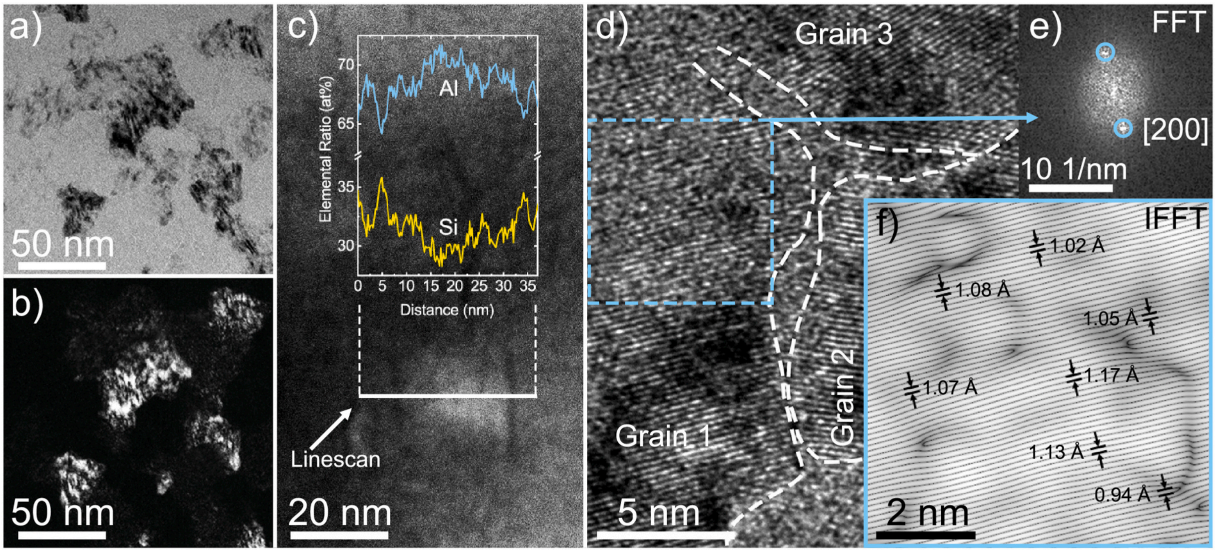

Fig. 3. Plan-view TEM-images of the HESN coating with 9.8 at.% in bright field (a), dark field (b), STEM-HAADF mode with an EELS linescan across one columnar grain (c), and a high resolution TEM-image of the highlighted junction between three crystalline grains (d). A fast Fourier transformation of the blue margined area in (d) reveals a single [200] oriented phase (e). The inverse fast Fourier transformation of the encircled spots in (e) reveals the distorted lattice planes and the high defect-density in more detail (f).

Fig. 3d shows the diffraction spots of a single grain in [200] orientation (Fig. 3e). The inverse fast Fourier transformation (IFFT) of the two selected spots in (Fig. 3e) reveals the distorted and defected lattice plains clearly in Fig. 3f. The indicated lattice plane distances (here we need to mention that we want to focus more on their variation and not on their individual numbers, as these measurements are obtained without an additional calibration) clearly show a wide variation and thereby a huge lattice distortion. Since the line density is doubled in the IFFT and the grain is [200] oriented, the line distances are roughly a quarter of the lattice parameter. Quadrupling the average of 1.07 Å yields a good agreement with the XRD measurement, based on which a lattice parameter of 4.30 Å was estimated for this coating. This supports the concept of severe lattice distortion not only in metallic high-entropy alloys but also in high-entropy metal-sublattice ceramics.

3.2. *Structure and phase stability*

The XRD measurements reveal a single-phased solid solution cubic structure for all coatings having 0 at.% Si (Fig. 4a), 6.4 at.% Si (Fig. 4b), 12.0 at.% Si (Fig. 4c), and 15.0 at.% Si (Fig. 4d) in the as-deposited state (bottom XRD pattern in black). The results confirm the SAED investigations and show that the addition of Si alters the preferred growth-orientation of the samples. Whereas the Si-free coating exhibits a more randomly oriented growth, with the [220] orientation being dominating, this changes with the addition of Si. The 6.4 at.% Si-containing coating exhibits a preferred [420]-oriented growth, and for the 12.0 and 15.0 at.% Si-containing coatings the [200] orientation is the preferred one. Our TEM investigations (Fig. 3) show that a small fraction of Si can be incorporated into the lattice, whereas higher Si contents

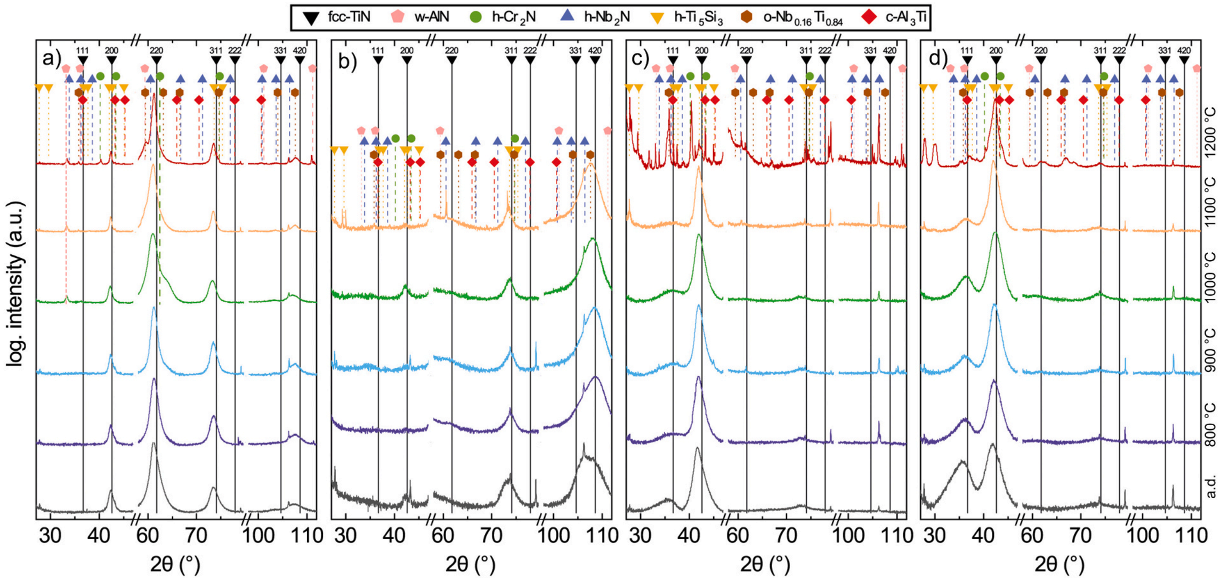

Fig. 4. XRD-patterns of as-deposited and vacuum annealed (Al,Cr,Nb,Ta,Ti)N coatings on sapphire with 0 at.% Si (a), 6.4 at.% Si (b), 12.0 at.% Si (c), and 15.0 at.% Si (d) show first decomposition products after annealing at 1000 °C for the Si-free coating (a). By Si-alloying, the decomposition onset is shifted up to 1200 °C. No XRD pattern could be recorded for the sample with 6.4 at.% Si after annealing at 1200 °C, due to a complete coating-spallation. The substrate peaks around 53 and 85° are cropped for better visibility.

promote segregation to the grain boundaries, which was also investigated for (Ti,Si)N [48,49]. We therefore attribute the texture changes to increased or decreased Si concentrations in the grains. The influence of Si on the peak shape is basically due to the reduction in coherently diffracting domain sizes (as presented in Fig. 1 as well). By increasing the Si-content, especially the column width becomes smaller, as seen in the SEM and TEM micrographs. The smaller coherently diffracting domain sizes lead to the formation of broader peaks, in addition, increased micro-stresses could contribute to broader peaks as well. From the SAED patterns we can conclude that only a single phase is present also in the Si-containing coatings.

The lattice parameter, simply estimated from the diffraction angle position and thus implying also contributions from stresses, increases from $a = 4.28$ to 4.34 Å with increasing Si content from 0 to 15.0 at.%. The lattice parameter is similar to TiN, which is also used for reference positions. This is despite the low total Ti concentration in the coatings. The approximate lattice parameters of the constituent fcc-structured binary components are 4.05, 4.14, 4.34, 4.34, and 4.24 Å for AlN (ICDD 00-046-1200), CrN (ICDD 01-076-2494), NbN (ICDD 01-071-0162), TaN (ICDD 00-049-1283), and TiN (ICDD 00-038-1420), respectively. Even though TiN makes up only a fraction of the coating, its lattice parameter lies between the lattice parameters of the other constituent metal nitrides.

Even after annealing in vacuum up to 900 °C all coatings remain in this single-phased solid solution. When comparing the Si-free coating with its Si-containing counterparts, the decomposition upon increasing the annealing temperature to 1000 °C and further, is clearly shifted to higher temperatures. Hereby, the samples containing 12.0 at.% and 15.0 at.% Si (Fig. 4c and d) show decomposition into w-AlN, intermetallic and other N-depleted phases earliest at 1200 °C. For better visibility, only a small selection of possible peaks and phases is marked in Fig. 4. The limiting factor for the phase stability is likely the tendency for CrN and TaN to release N_2 and form Cr_2N above 900 °C, and Ta_2N at 1100 °C, enabling subsequent reactions to take place [50,51]. Please note that the sample with 12.0 at.% Si (Fig. 4c) suffered from severe spallation during/after annealing to 1200 °C, so that only a careful XRD measurement but no nanoindentation test could be performed.

3.3. Mechanical properties

In Fig. 5, the hardness (H) of the Si-free and Si-containing coatings depending on the annealing temperature is shown. In the as-deposited state, the addition of Si increases the hardness starting from 32.6 ± 2.0 GPa without Si to 34.3 ± 1.0 GPa and 35.4 ± 1.1 GPa for samples with 6.4 at.% and 9.8 at.% Si, respectively. This can be attributed to the smaller grain size, changes in bond-characteristics, and increased cohesive strength of the grain boundaries [52] due to the addition of Si (see Fig. 2). Exceeding this Si content, the hardness drastically drops to ≈24 GPa (coatings with 12.0 and 15.0 at.% Si). During vacuum annealing at 800 °C the hardness of all coatings increases by ≈2 GPa. Hereby, an exception is drawn by the coating containing 12.0 at.% Si, which shows a tremendous increase from 24.5 ± 0.6 to 37.3 ± 0.9 GPa when annealed at 800.

Based also on previous investigations and reports, and because the XRD investigations do not show significant changes upon annealing to these temperatures (Fig. 4c), we attribute this to the compaction of the amorphous-like Si-rich grain boundaries, where parts may even be built into the surrounded or encapsulated grains, which increases the cohesive strength of the grain boundaries [49,48,53]. Note, that this is different from a full crystallization of amorphous Si-nitride, which happens above 1200 °C [54]. The addition of Si to transition metal nitrides is known to result in the formation of small grains and high cohesive strengths of the grain boundaries [48].

Coatings with a Si content between 6.4 and 12.0 at.% retain their high hardness until $T_a = 1100$ ° C. For $T_a = 1200$ ° C delamination of the films impedes their investigation by nanoindentation. Only the Si-free and the 15.0 at.% Si-containing thin films could be evaluated after annealing at $T_a = 1200$ ° C, showing rather contrary results. Whereas the Si-free coating retains its hardness of 31.0 ± 1.6 GPa, the hardness of the coating with the highest Si content drops to ≈8 GPa. This coating shows a massive change in crystal structure and phase composition due to a severe loss of nitrogen (Fig. 4d). However, the hardness retention of the lower Si-containing coatings during annealing at high temperatures is remarkable for a single-phase coating. Unlike single-phase binaries, e.g., TiN, our high-entropy metal-sublattice nitride (Al,Cr,Nb,Ta,Ti)N with and without Si does not easily undergo recovery processes (where lattice defects arrange towards lower-energy sites), since the many elements with hugely different sizes at the metal-sublattice distort the lattice (Fig. 3d and f), allowing only for reduced diffusion [31]. Thus, the hardness is retained even when annealed at high temperatures due to sluggish diffusion.

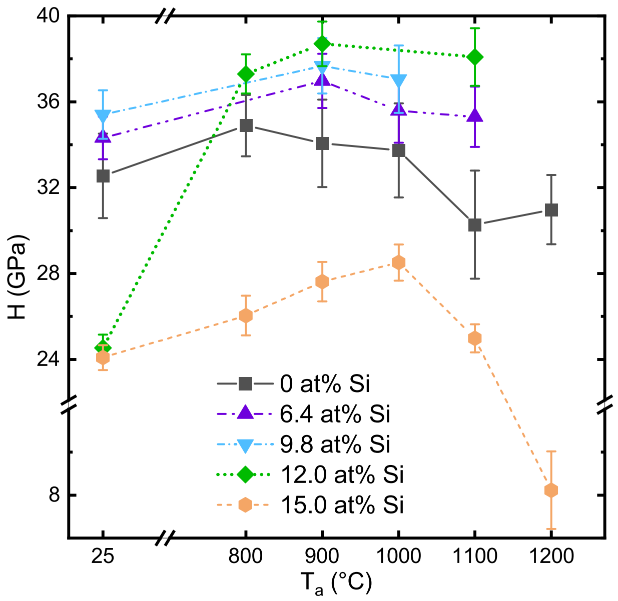

Fig. 5. Indentation hardness, H, of the HESN coatings with and without Si-alloying in the as-deposited state and after vacuum annealing at T_a up to 1200 °C. Missing data points after annealing at 1100 and/or 1200 °C are due to complete spallation of the coating from their sapphire substrate due to the annealing treatment. The standard deviations are given as error bars.

For the HESN coatings without Si, the indentation modulus lies between 445 ± 25 and 519 ± 20 GPa for all annealing temperatures. In as-deposited state, the indentation modulus of our coatings decreases by more than 100GPa with increasing Si-content. After annealing at 1100 °C, the coatings with 0, 6.4, 9.8, and 12.0 at.% Si show similar indentation moduli of around 440 GPa. The highest Si-containing coating (with 15.0 at.% Si) is again off the trend, with values below 363 ± 12 GPa. Importantly to mention, with increasing Si-content up to 12.0 at.% the hardness increases especially if the coatings are annealed at $T_a = 800$–1100 °C (Fig. 5). With Si addition the indentation modulus is lowered (Fig. 6). Combining higher hardness with lower indentation modulus leads to higher H/E or H^3/E^2 ratios - two parameters often used to rate coatings within a series for their wear performance [55] - indicating higher elasticity behavior. Indeed, as shown by in-situ micromechanical cantilever bending tests of another high-entropy sublattice nitride, (Al,Ta,Ti,V,Zr)N, Si had nearly no impact on the fracture toughness (for the Si content tested up to 4.9 at.%), but allowed for an increased area under the linear-elastic region of the stress-intensity-bending-strain curve, indicative for an increased damage tolerance [56].

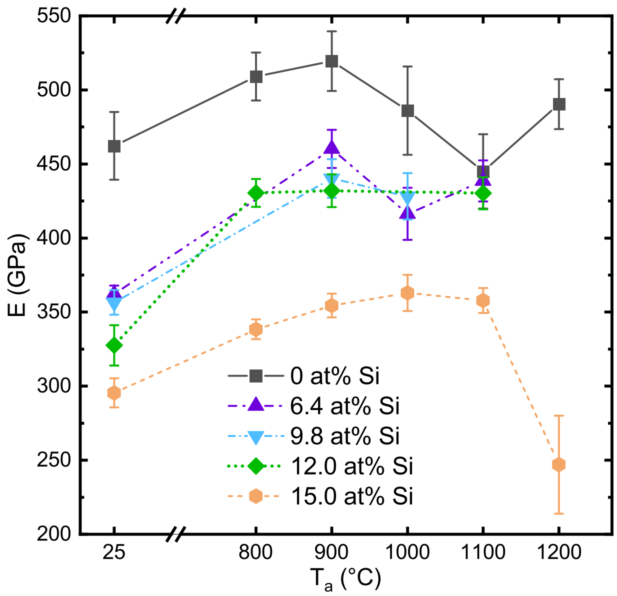

Fig. 6. Indentation modulus, *E*, of the HESN coating with and without Si-alloying in the as-deposited state and after vacuum annealing at T_a up to 1200 °C. Missing data points after annealing at 1100 and/or 1200 °C are due to complete spallation of the coating from their sapphire substrate due to the annealing treatment. The standard deviations are given as error bars.

3.4. Oxidation resistance

In Fig. 7 the XRD patterns of gradually oxidized samples with different Si concentrations are shown. Fig. 7a features an overview of the Si-free high-entropy metal-sublattice (Al,Cr,Nb,Ta,Ti)N coating before and after oxidation at 850 °C for 100 h. Clearly, a rutile-structured oxide is formed, but the nitride is still present in its single-phase cubic form. While in a powder the (110) peak at 27.1° possesses the highest intensity, it is only a very weak reflex in our oxide scales due to their strong texture. The highlighted (101) and (112) peaks have the highest intensities of all oxide peaks that do not overlap with a substrate or nitride signal. No other oxide phases could be detected, indicating the formation of a single-phase rutile-structured solid solution oxide from the single-phase fcc-structured high-entropy metal-sublattice ($Al_{0.20}Cr_{0.26}Nb_{0.15}Ta_{0.16}Ti_{0.23}$)N coating. Out of the metals present, Al is the only reported to form no rutile structured oxide (there are metastable rutile-structured oxides for Cr, Nb, and Ta). Therefore, our experimental data suggest that also the Al is soluted in the structure, enabled by the many other metals forming a solid solution rutile oxide.

This could also be confirmed with DFT calculations. The free mixing enthalpy between rutile-structured solid solution (Al,Cr,Nb,Ta,Ti)O_2 and its stable binary metal-oxides (which are all non-rutile structured except for TiO_2) is −1.23 eV/atom; clearly designating the solid solution (Al,Cr,Nb,Ta,Ti)O_2 energetically more preferred over the individual binary metal-oxides. Entropic effects would further support this high-entropy metal-sublattice dioxide over the individual binaries. When calculating all possible isostructural decomposition products of the (Al,Cr,Nb,Ta,Ti)O_2 solid solution, the most likely ones are (Al,Ta,Ti)O_2 and (Cr,Nb)O_2. But with $\Delta G_{mix} = 0.00984$ eV/at at 0 K (between the (Al,Cr,Nb,Ta,Ti)O_2 and these products), the driving force for such a decomposition is extremely small and could easily be consumed by any nucleation barrier or strain formation. Even without these retarding energies that are typically present during decomposition, already above 509 K, ΔG_{mix} becomes negative due to the higher entropy of the (Al,Cr,Nb,Ta,Ti)O_2 solid solution than the product phases. Hence, entropy stabilization is easily reached for such an isostructural decomposition scenario. But even more important for our oxidation scenario, the single-phased solid solution will form rather than individual oxide phases during the 850 °C oxidation experiment. Upon cooling, especially below 509 K where ΔG_{mix} would become positive, limited kinetics guarantee for the kinetic stabilization of the high-entropy metal-sublattice dioxide (Al,Cr,Nb,Ta,Ti)O_2.

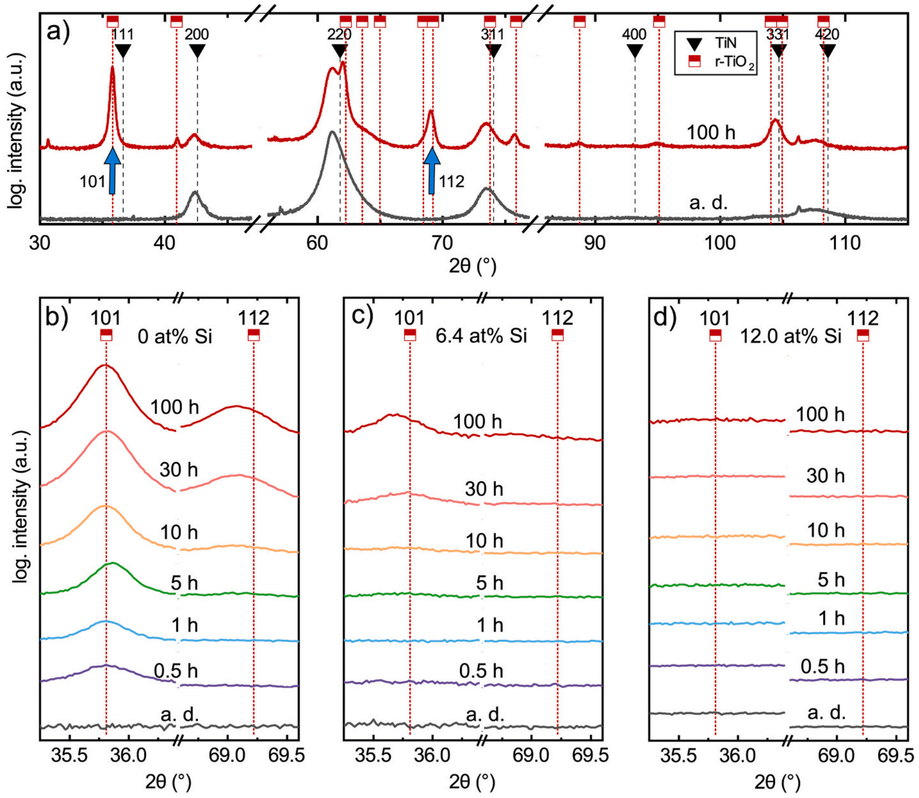

Fig. 7. (a) XRD patterns of the Si-free HESN coating in its as-deposited (a. d.) state and after exposure to ambient air at 850 °C for 100 h. The standard peak positions for TiN and rutile-structured TiO_2 (r-TiO_2) are indicated with black triangles and red squares, respectively. Details of the XRD regions around the dominating (101) and (112) peaks of r-TiO_2 (indicated by blue arrows) for the HESN coatings without Si, with 6.4 at.% Si, and with 12.0 at.% Si are given in (b), (c), and (d), respectively, after the ambient-air exposure at 850 °C for 0, 0.5, 1, 5, 10, 30, and 100 h. As-deposited coatings do not show any signal (other than the background) in this range.

Kirnbauer et al. [22] developed a single-phase rutile-structured high-entropy metal-sublattice dioxide of a similar composition $(Al_{0.19}Cr_{0.13}Nb_{0.19}Ta_{0.30}Ti_{0.19})O_2$ by reactive magnetron sputtering, which stayed single-phase rutile-structured even when annealed at 1200 °C. Developing a single-phase multi-elemental dioxide by PVD is taking advantage of kinetic limitations during PVD allowing to stretch the solubility-limits. But here we could show that the Al-containing solid solution rutile-structured dioxide forms by thermodynamic means during the oxidation of the HESN at 850 °C. The time-dependent development of this rutile-structured dioxide at the $(Al_{0.20}Cr_{0.26}Nb_{0.15}Ta_{0.16}Ti_{0.23})N$ is shown with the (101) and (112) XRD peaks in Fig. 7b. The corresponding XRD patterns for the 6.4 at.% Si-containing coating, Fig. 7c, clearly show significantly lower-intensity XRD peaks. For 12.0 at.% Si (Fig. 7d) as well as for 15.0 at.% Si (not shown) no crystalline oxide peaks could be detected even after 100 h exposure at 850 °C, suggesting for a significantly retarded oxidation process or the formation of an XRD-amorphous oxide.

With cross-sectional SEM investigations of the coatings after 1, 10, 30, and 100 h oxidation at 850 °C (for the Si-free coating also after 5 h), we investigated the oxide-scale thickness evolution. Exemplarily this is shown for the Si-free and 6.4 at.% Si-containing sample after 100 h in Fig. 8a and b, respectively. While the Si-free coating exhibits a 2700 nm thick oxide scale, the Si-alloyed coatings show only a 280 nm thin oxide scale. Also, EDS-line-scans are conducted proving the relative homogeneous chemistry of the growing oxide across the scale thickness (especially for the Si-free sample). Furthermore important to mention is that the relative metal content within the remaining nitride is very similar to that in the growing oxide. For all oxide scales investigated, the elemental distribution of metals in the oxide scale is comparable to the samples shown in the manuscript. The only inhomogeneity detectable by SEM-EDS in the oxide scale is the O content that increases near the surface. The relatively long oxidation time of 100 h allows for an accurate determination of the oxidation kinetics derived from evaluating the time-dependent oxide-scale thickness, plotted in Fig. 8c. The oxidation kinetic for the scale growth on the Si-free sample, $(Al_{0.20}Cr_{0.26}Nb_{0.15}Ta_{0.16}Ti_{0.23})N$, can best be described by parabolic behavior, whereas all Si-alloyed samples follow a logarithmic growth kinetic. The respective equations for the oxide thickness *x* as a function of time *t*, developed by Tammann [57,58], are

$$x^2 = k_p \cdot t + C_p \tag{4}$$

and

$$x = k_l \cdot log(C_l \cdot t + B), \tag{5}$$

with k_p k_l are the parabolic and logarithmic rate constants, respectively, and C_p, C_l, and B corresponding constants. The parabolic rate constant for the Si-free HESN at 850 °C is $k_p = (2.1 \pm 0.1) \cdot 10^{-17} m^2 s^{-1}$ with $C_p = (-1.4 \pm 2.2) \cdot 10^{-14} m^2$. As mentioned, all Si-alloyed HESN coatings follow a logarithmic oxide scale growth with a rate constant k_l of about $(7.2 \pm 0.9) \cdot 10^{-8}$ m, and $C_l = (1.5 \pm 1.3) \cdot 10^{-2} s^{-1}$ and $B = 1.0 \pm 0.5$. Shen et al. [16], suspected already a logarithmic oxide growth behavior for their Si-containing $(Al_{0.34}Cr_{0.22}Nb_{0.11}Si_{0.11}Ti_{0.22})_{50}N_{50}$ at 900 °C. Oxidizing our Si-containing coatings (having a slightly different chemical composition, e.g., $(Al_{0.17}Cr_{0.25}Nb_{0.15}Si_{0.15}Ta_{0.12}Ti_{0.16})N$ for the 6.4 at.% Si-containing case) for a much longer time (100 h) allowed us to confirm the logarithmic growth kinetic. The SEM cross sections of the oxidized Si-containing coatings show that the oxide scale thickness stays roughly the same between the different Si concentrations. Since the oxide peaks diminish with higher Si concentrations (Fig. 7c and d) this is a clear indication that higher Si concentrations allow the formation of a more dense amorphous oxide scale. The results clearly show that already the 6.4 at.% Si-containing coating, $(Al_{0.17}Cr_{0.25}Nb_{0.15}Si_{0.15}Ta_{0.12}Ti_{0.16})N$, shows an exceptional oxidation resistance. While the addition of more Si does not markedly improve the oxidation resistance further, it influences the mechanical properties (Figs. 5 and 6).

This oxidation resistance is superior to two comparable nitride coatings with lower metal-sublattice entropy, $Ti_{0.45}Al_{0.36}Ta_{0.19}N$ and $Ti_{0.41}Al_{0.56}Ta_{0.03}N$, that were oxidized for 20 h in 850 °C hot air and yielded oxide scale thicknesses of ≈1000 and 750 nm, respectively [5,59]. (Ti,Al)N coatings (~4 μm thick), also investigated in both studies, were fully oxidized under the same conditions.

Detailed TEM investigations show that the growing oxide scale becomes significantly denser when Si is present. Bright-field and dark-field TEM cross-sections of the Si-free sample after 100 h at 850 °C in air are given in Fig. 9a and b, respectively. This sample shows a rather sharp

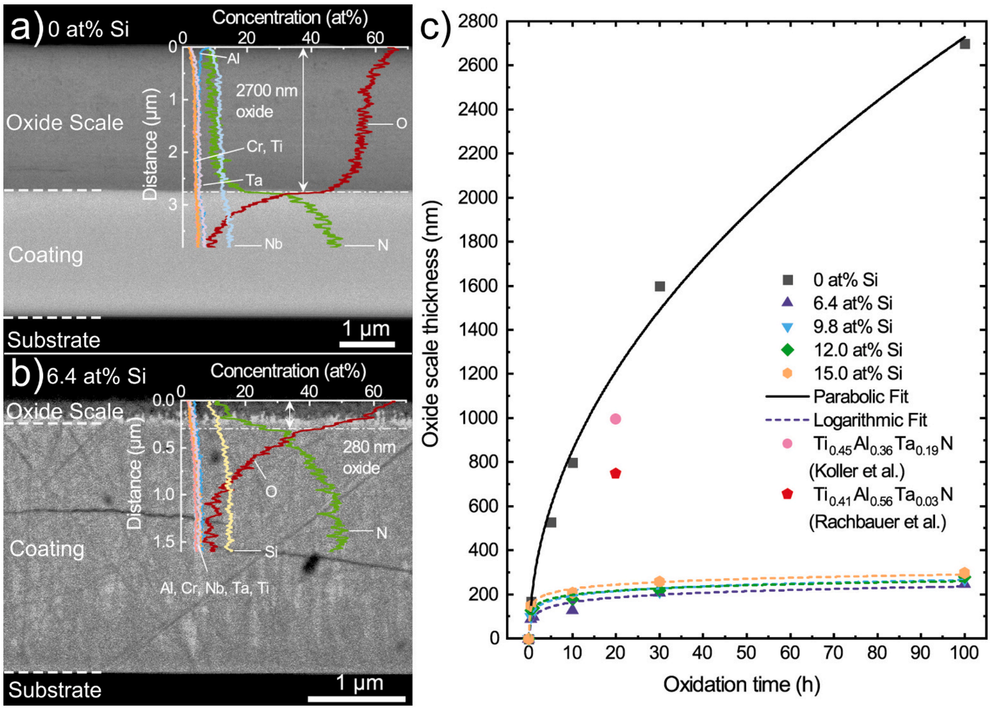

Fig. 8. SEM cross-section of the HESN coating without Si (a) and with 6.4 at.% Si (b) after exposure to ambient air at 850 °C for 100 h. The recorded EDS-linescans across the oxide scale are placed directly to the corresponding part. The oxide scale thickness evolution with time at 850 for all HESN coatings investigated (with 0, 6.4, 9.8, 12.0, and 15.0 at.% Si) is presented in (c). For comparison, also the oxide scale thickness of $Ti_{0.45}Al_{0.36}Ta_{0.19}N$ [5] and $Ti_{0.41}Al_{0.56}Ta_{0.03}N$ [59] coatings on sapphire after 20 h at 850 °C is added. Note that the Si content in (b) is overestimated due to the interaction between Si and Ta EDS signals.

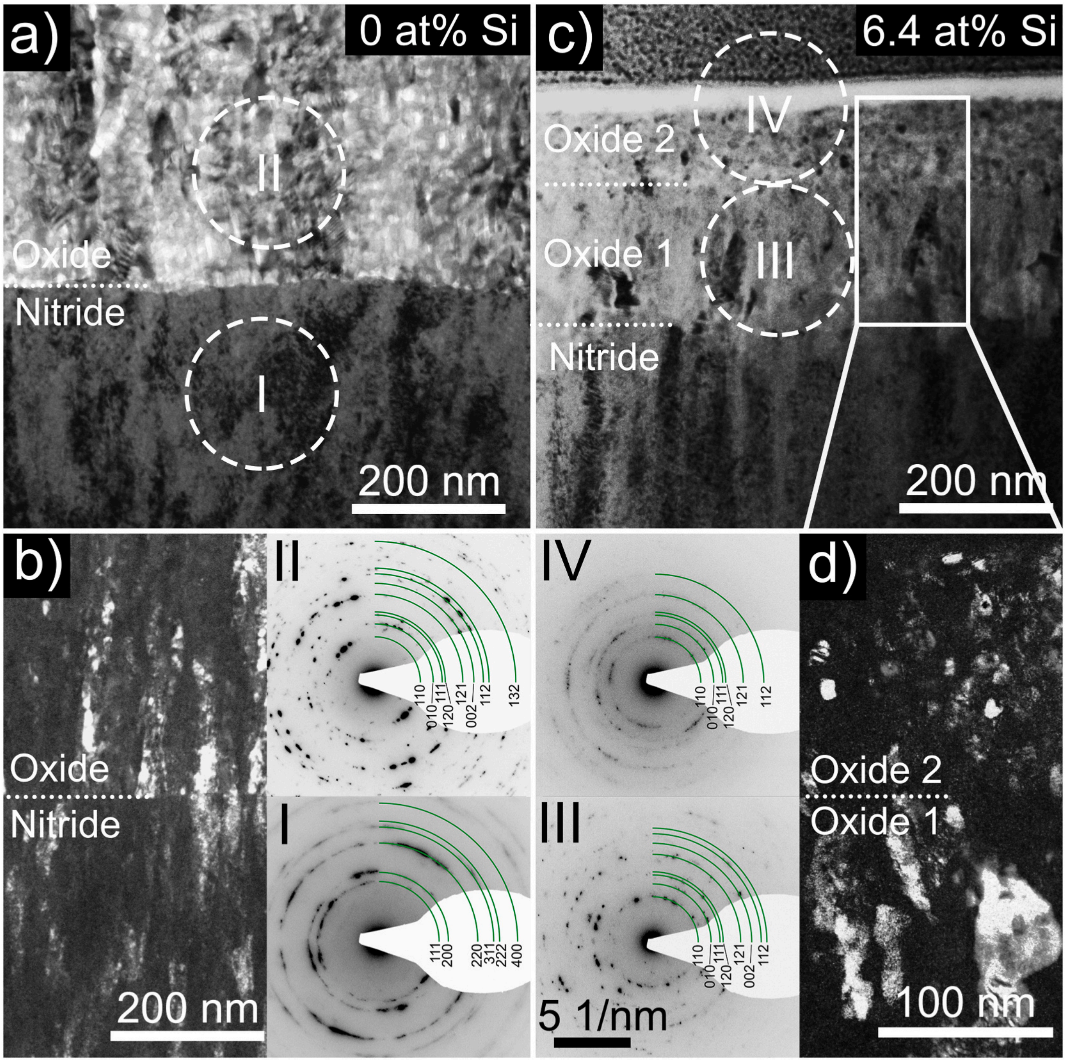

Fig. 9. Cross-sectional TEM investigations of the HESN coating without Si (a) and (b), and with 6.4 at.% Si (c) and (d) after oxidation in air at 850 °C for 100 h. (a) and (c) are BF, and (b) and (d) are DF TEM studies. The areas used for SAED are indicated in (a) and (c) by dashed white circles and labeled with (I), (II), (III), and (IV). The remaining nitride is still single-phase fcc rock-salt structured (SAED inset I), and all oxide regions indicate a single-phase rutile structure (SAED insets I, II, and III).

interface between nitride and growing oxide scale and interestingly, the columnar grains of the nitride are neatly continued into the oxide scale, Fig. 9b. SAED patterns taken from selected regions within the nitride and the growing oxide, indicated with (I) and (II) in Fig. 9a, show a single-phase fcc solid solution for the remaining nitride, and a single-phase rutile-structured solid solution for the oxide. Thus, these investigations support the conclusions derived from the XRD investigations (Fig. 7a). The rather distinct diffraction spots of the oxide pattern (Fig. 9b-II) indicate larger grains than within the nitride, which leads to a more ring-like SAED pattern (Fig. 9b-I).

When Si is alloyed to the HESN, the interface between nitride and growing oxide is blurred, and within the oxide two regions can be distinguished, Fig. 9c. The nitride-near region basically resembles the columnar grain structure of the HESN and the outer region exhibits more equiaxed grains with a much smaller average size, as proven by dark field investigations, Fig. 9d. However, both regions are single-phase rutile structured, see the corresponding SAED patterns (III) and (IV) given in Fig. 9d. The smaller grains of the outer oxide lead to a more ring-like SAED pattern (IV).

STEM investigations clearly show the blurred transition between Si-containing HESN and the growing oxide, Fig. 10a. After the transition zone - which is about 100 nm thick and where the O signal increases and the N signal decreases - the O content is about 63 at.%. This inner oxide shows almost no Cr, which is more concentrated in the outer oxide having also a higher O content of about 68 at.%. The Si content almost gradually decreases from a high value (at the interface to the remaining nitride) to a small one at the outer surface, where the Al content is highest. Also the Si-free sample shows an Al-rich and O-rich outermost region of the growing oxide scale, compare Fig. 8a. We could not detect any crystalline corundum in any oxidized coating neither by XRD or SAED, meaning that this Al-oxide layer is amorphous. The elements Nb and Ta are not given in the EDS line scan as their signals are essentially constant at ≈2 at.% across the entire scan through nitride and oxide. The STEM image furthermore suggests that the outer oxide contains significantly more pores than the inner one. Thus, especially the inner oxide is able to be an effective diffusion barrier against further oxidation. The coating without Si leads to the formation of an oxide with much larger pores, Fig. 10b, up to 30 nm in diameter. Here, no denser sub-layer oxide is present and therefore also the oxidation kinetic is faster.

4. Conclusions

Alloying the reactively magnetron sputtered high-entropy sublattice nitride (Al,Cr,Nb,Ta,Ti)N with Si improves the performance under

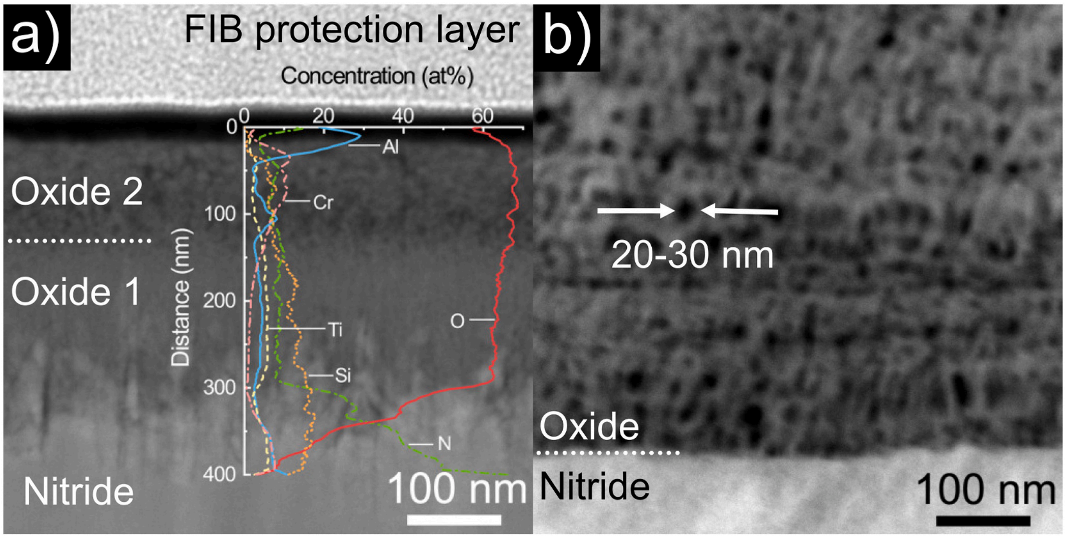

Fig. 10. STEM investigations of the HESN coating with 6.4 at.% Si (a), and without Si (b) after exposure to ambient air at 850 °C for 100 h. The STEM EDS line scan across the oxide scale grown on the 6.4 at.% Si-containing coating is added directly to the STEM cross-section in (a). For the Si-containing HESN, a gradual transition between remaining nitride and growing oxide is present (a). Also, the oxide itself has gradual changes in morphology and Si as well as Cr contents. The inner Si-rich region is denser than the outer Cr-rich region, which even shows small pores. The O content increases from 63 to 68 at.% towards the outer surface. Nb and Ta signals (constant at ~2 at.%) are excluded for better visibility, and the Si content is overestimated due to interaction with the Ta EDS signal. The Si-free HESN shows a much sharper interface between remaining nitride and growing oxide and also larger pores with diameters up to 30 nm. Here, the oxide scale itself is rather homogeneous in morphology and chemistry, except for the Al-and O-rich outermost region (not shown, see Fig. 8).

thermal and mechanical loading, and oxidative attack. Increasing the Si-content changes the coating morphology to finer and longer columns. All coatings exhibit single-phase solid solutions in fcc rock-salt structure, with lattice parameters increasing from 4.28 to 4.34 Å with increasing Si content. Upon vacuum annealing, this crystal structure was maintained until decomposition reactions set in at 1000 °C for the Si-free material. By Si-alloying the decomposition is shifted to higher temperatures and starts at about 1200 °C for the coating with 12.0 at.% Si. Si-enrichment at the grain boundaries as well as the severe lattice distortion (one of the core-effects of high-entropy materials) were determined by TEM-studies.

With increasing Si content to 9.8 at.% the hardness of as-deposited coatings increases from 32 to 35 GPa. A further increase in Si causes a hardness drop to 24 GPa, which for the 12.0 at.% Si-containing coating can be reversed into a hardness increase to 37 GPa upon a subsequent vacuum annealing to 800 °C. Also, the other coatings (except for the highest Si-containing one with 15.0 at.% Si) experience a hardness increase (to a smaller extent) upon annealing. The indentation modulus decreases with increasing Si content from 470 to 350 GPa.

Upon exposure to ambient air at 850 °C for 100 h, a single-phase rutile-structured oxide grows on the Si-free (Al,Cr,Nb,Ta,Ti)N coating with a parabolic growth rate k_p of 2.110^{-17} m/s. The formation of a single-phase multielemental dioxide is supported by DFT calculations of an equimolar $(Al,Cr,Nb,Ta,Ti)O_2$, which is energetically more stable than the formation of the respective binary oxides (in the thermodynamically most stable configuration). Only the formation of a rutile-structured mixture of $(Al,Ta,Ti)O_2$ and $(Cr,Nb)O_2$ would be more favorable than the single-phase solid solution. But the higher entropy of the solid solution $(Al,Cr,Nb,Ta,Ti)O_2$ ensures that already above 509 K its formation is preferred over these mixtures.

The Si-containing HESN coatings exhibit a significantly reduced oxide scale growth kinetic, which at 850 °C can best be described with a logarithmic function of $k_l = 7.2 \times 10^{-8}$ m, independent on the Si content investigated (between 6.4 and 15.0 at.%). Although, also here no different crystalline oxide phases could be identified, the oxide scale morphology is divided into a denser Si-rich inner oxide and a slightly more porous Cr-rich outer scale. Without Si, the oxide scale morphology is more uniform throughout the entire thickness but also more porous with pore diameters up to 30 nm. Our results suggest that especially the inner Si-rich but Cr-lean oxide scale, which is rather dense and well adherent without a sharp transition to the underlying nitride, guarantees for the excellent oxidation resistance of the Si-containing HESN (in addition to the thin, dense outermost Al-rich oxide).

CRediT authorship contribution statement

Andreas Kretschmer: Conceptualization, Software, Visualization, Investigation, Formal analysis, Writing – original draft. **Alexander Kirnbauer:** Conceptualization, Formal analysis, Writing – review & editing. **Vincent Moraes:** Investigation, Formal analysis, Writing – original draft. **Daniel Primetzhofer:** Resources, Formal analysis, Funding acquisition, Writing – review & editing. **Kumar Yalamanchili:** Project administration, Writing – review & editing. **Helmut Rudigier:** Funding acquisition. **Paul Heinz Mayrhofer:** Project administration, Funding acquisition, Resources, Supervision, Writing – original draft.

Declaration of competing interest

The authors declare no competing interests.

Acknowledgements

This work was funded by the Austrian COMET Program (project K2 InTribology1, no. 872176). Operation of the accelerator at Uppsala University was supported by the Swedish Research Council VR-RFI (Contracts No. 2017-00646_9) and the Swedish Foundation for Strategic Research (Contract No. RIF14-0053). The computational results presented have been achieved using the Vienna Scientific Cluster (VSC). The authors acknowledge the use of the X-ray center (XRC) and USTEM at TU Wien. They are also very grateful to Philip Kutrowatz (TU Wien, Austria) for TEM sample preparation and Tomasz Wojcik (TU Wien, Austria) for assistance with TEM investigations and valuable discussions. A. Kretschmer thanks David Holec (Montanuniversität Leoben) for advice on computations. Plansee Composite Materials GmbH is acknowledged for supplying target materials. The authors acknowledge TU Wien Bibliothek for financial support through its Open Access

Funding Programme.

References

[1] M. Wittmer, J. Noser, H. Melchior, Oxidation kinetics of TiN thin films, J. Appl. Phys. 52 (11) (1981) 6659–6664, https://doi.org/10.1063/1.328659.

[2] P.C. Jindal, A.T. Santhanam, U. Schleinkofer, A.F. Shuster, Performance of PVD TiN, TiCN, and TiAlN coated cemented carbide tools in turning, Int. J. Refract. Met. Hard Mater. 17 (1) (1999) 163–170, https://doi.org/10.1016/S0263-4368(99)00008-6.

[3] J.L. Mo, M.H. Zhu, B. Lei, Y.X. Leng, N. Huang, Comparison of tribological behaviours of AlCrN and TiAlN coatings-deposited by physical vapor deposition, Wear 263 (7–12 SPEC. ISS) (2007) 1423–1429, https://doi.org/10.1016/j.wear.2007.01.051.

[4] J.L. Mo, M.H. Zhu, A. Leyland, A. Matthews, Impact wear and abrasion resistance of CrN, AlCrN and AlTiN PVD coatings, Surf. Coat. Technol. 215 (2013) 170–177, https://doi.org/10.1016/j.surfcoat.2012.08.077.

[5] C.M. Koller, R. Hollerweger, C. Sabitzer, R. Rachbauer, S. Kolozsvári, J. Paulitsch, P.H. Mayrhofer, Thermal stability and oxidation resistance of arc evaporated TiAlN, TaAlN, TiAlTaN, and TiAlN/TaAlN coatings, Surf. Coat. Technol. 259 (PC (2014) 599–607, https://doi.org/10.1016/j.surfcoat.2014.10.024.

[6] M. Kawate, A.K. Hashimoto, T. Suzuki, Oxidation resistance of $Cr_{1-x}Al_xN$ and $Ti_{1-x}Al_xN$ films, Surf. Coat. Technol. 165 (2) (2003) 163–167, https://doi.org/10.1016/S0257-8972(02)00473-5.

[7] J. L. Endrino, V. Derflinger, The influence of alloying elements on the phase stability and mechanical properties of AlCrN coatings, Surface and Coatings Technology 200 (1–4 SPEC. ISS.) (2005) 988–992. doi:https://doi.org/10.1016/j.surfcoat.2005.02.196.

[8] B. Cantor, I. T. Chang, P. Knight, A. J. Vincent, Microstructural development in equiatomic multicomponent alloys, Materials Science and Engineering A 375–377 (1–2 SPEC. ISS.) (2004) 213–218. doi:https://doi.org/10.1016/j.msea.2003.10.257.

[9] J. W. Yeh, S. K. Chen, S. J. Lin, J. Y. Gan, T. S. Chin, T. T. Shun, C. H. Tsau, S. Y. Chang, Nanostructured high-entropy alloys with multiple principal elements: novel alloy design concepts and outcomes, Advanced Engineering Materials 6 (5) (2004) 299–303+274. doi:https://doi.org/10.1002/adem.200300567.

[10] J.W. Yeh, Alloy design strategies and future trends in high-entropy alloys, Jom 65 (12) (2013) 1759–1771, https://doi.org/10.1007/s11837-013-0761-6.

[11] D.B. Miracle, J.D. Miller, O.N. Senkov, C. Woodward, M.D. Uchic, J. Tiley, Exploration and development of high entropy alloys for structural applications, Entropy 16 (1) (2014) 494–525, https://doi.org/10.3390/e16010494.

[12] D.B. Miracle, O.N. Senkov, A critical review of high entropy alloys and related concepts, Acta Mater. 122 (2017) 448–511, https://doi.org/10.1016/j.actamat.2016.08.081.

[13] B. Murty, J.W. Yeh, S. Ranganathan, High Entropy Alloys, Elsevier, 2014, https://doi.org/10.1016/C2013-0-14235-3.

[14] P.H. Mayrhofer, A. Kirnbauer, P. Ertelthaler, C.M. Koller, High-entropy ceramic thin films; a case study on transition metal diborides, Scr. Mater. 149 (2018) 93–97, https://doi.org/10.1016/j.scriptamat.2018.02.008.

[15] A. Kirnbauer, A. Kretschmer, C.M. Koller, T. Wojcik, V. Paneta, M. Hans, J. M. Schneider, P. Polcik, P.H. Mayrhofer, Mechanical properties and thermal stability of reactively sputtered multi-principal-metal Hf-Ta-Ti-V-Zr nitrides, Surf. Coat. Technol. 389 (March) (2020) 125674, https://doi.org/10.1016/j.surfcoat.2020.125674.

[16] W. J. Shen, M. H. Tsai, K. Y. Tsai, C. C. Juan, C. W. Tsai, J. W. Yeh, Y. S. Chang, Superior oxidation resistance of (Al0.34Cr0.22Nb0.11Si0.11Ti0.22)50N50high-entropy nitride, Journal of the Electrochemical Society 160 (11) (2013) 531–535. doi:https://doi.org/10.1149/2.028311jes.

[17] Q.W. Xing, S.Q. Xia, X.H. Yan, Y. Zhang, Mechanical properties and thermal stability of (NbTiAlSiZr)Nx high-entropy ceramic films at high temperatures, J. Mater. Res. 33 (19) (2018) 3347–3354, https://doi.org/10.1557/jmr.2018.337.

[18] T.H. Hsieh, C.H. Hsu, C.Y. Wu, J.Y. Kao, C.Y. Hsu, Effects of deposition parameters on the structure and mechanical properties of high-entropy alloy nitride films, Curr. Appl. Phys. 18 (5) (2018) 512–518, https://doi.org/10.1016/j.cap.2018.02.015.

[19] T.J. Harrington, J. Gild, P. Sarker, C. Toher, C.M. Rost, O.F. Dippo, C. McElfresh, K. Kaufmann, E. Marin, L. Borowski, P.E. Hopkins, J. Luo, S. Curtarolo, D. W. Brenner, K.S. Vecchio, Phase stability and mechanical properties of novel high entropy transition metal carbides, Acta Mater. 166 (2019) 271–280, https://doi.org/10.1016/j.actamat.2018.12.054.

[20] E. Chicardi, C. García-Garrido, F.J. Gotor, Low temperature synthesis of an equiatomic (TiZrHfVNb)C5 high entropy carbide by a mechanically-induced carbon diffusion route, Ceram. Int. 45 (17) (2019) 21858–21863, https://doi.org/10.1016/j.ceramint.2019.07.195.

[21] J.K. Xiao, H. Tan, J. Chen, A. Martini, C. Zhang, Effect of carbon content on microstructure, hardness and wear resistance of CoCrFeMnNiCx high-entropy alloys, J. Alloys Compd. 847 (2020) 156533, https://doi.org/10.1016/j.jallcom.2020.156533.

[22] A. Kirnbauer, C. Spadt, C.M. Koller, S. Kolozsvári, P.H. Mayrhofer, High-entropy oxide thin films based on Al–Cr–Nb–Ta–Ti, Vacuum 168 (July) (2019) 108850, https://doi.org/10.1016/j.vacuum.2019.108850.

[23] D. Wang, S. Jiang, C. Duan, J. Mao, Y. Dong, K. Dong, Z. Wang, S. Luo, Y. Liu, X. Qi, Spinel-structured high entropy oxide (FeCoNiCrMn)3O4 as anode towards superior lithium storage performance, J. Alloys Compd. 844 (2020) 156158, https://doi.org/10.1016/j.jallcom.2020.156158.

[24] J. Gild, Y. Zhang, T. Harrington, S. Jiang, T. Hu, M.C. Quinn, W.M. Mellor, N. Zhou, K. Vecchio, J. Luo, High-entropy metal diborides: a new class of high-entropy materials and a new type of ultrahigh temperature ceramics, Sci. Rep. 6 (October) (2016) 2–11, https://doi.org/10.1038/srep37946.

[25] X. Q. Shen, J. X. Liu, F. Li, G. J. Zhang, Preparation and characterization of diboride-based high entropy (Ti0.2Zr0.2Hf0.2Nb0.2Ta0.2)B2–SiC particulate composites, Ceramics International 45 (18) (2019) 24508–24514. doi:https://doi.org/10.1016/j.ceramint.2019.08.178.

[26] A. Kirnbauer, A. Wagner, V. Moraes, D. Primetzhofer, M. Hans, J. Schneider, P. Polcik, P. Mayrhofer, Thermal stability and mechanical properties of sputtered (Hf, Ta,V,W,Zr)-diborides, Acta Materialia (sep 2020). doi:https://doi.org/10.1016/j.actamat.2020.09.018.

[27] L. Liu, L. Zhang, D. Liu, Complete elimination of pest oxidation by high entropy refractory metallic silicide (Mo0.2W0.2Cr0.2Ta0.2Nb0.2)Si2, Scr. Mater. 189 (2020) 25–29, https://doi.org/10.1016/j.scriptamat.2020.07.059.

[28] Y. Qin, J.C. Wang, J.X. Liu, X.F. Wei, F. Li, G.J. Zhang, C. Jing, J. Zhao, H. Wu, High-entropy silicide ceramics developed from (TiZrNbMoW)Si2 formulation doped with aluminum, J. Eur. Ceram. Soc. 40 (8) (2020) 2752–2759, https://doi.org/10.1016/j.jeurceramsoc.2020.02.059.

[29] P.K. Huang, J.W. Yeh, Effects of substrate temperature and post-annealing on microstructure and properties of (AlCrNbSiTiV)N coatings, Thin Solid Films 518 (1) (2009) 180–184, https://doi.org/10.1016/j.tsf.2009.06.020.

[30] P.K. Huang, J.W. Yeh, Inhibition of grain coarsening up to 1000 Â°C in (AlCrNbSiTiV)N superhard coatings, Scr. Mater. 62 (2) (2010) 105–108, https://doi.org/10.1016/j.scriptamat.2009.09.015.

[31] S.Y. Chang, Y.C. Huang, C.E. Li, H.F. Hsu, J.W. Yeh, S.J. Lin, Improved diffusion-resistant ability of multicomponent nitrides: from unitary TiN to senary high-entropy (TiTaCrZrAlRu)N, Jom 65 (12) (2013) 1790–1796, https://doi.org/10.1007/s11837-013-0676-2.

[32] P. Kumar, S. Avasthi, Diffusion barrier with 30-fold improved performance using AlCrTaTiZrN high-entropy alloy, J. Alloys Compd. 814 (2020) 151755, https://doi.org/10.1016/j.jallcom.2019.151755.

[33] R. Li, B. Qiao, H. Shang, J. Zhang, C. Jiang, W. Zhang, Multi-component AlCrTaTiZrMo-nitride film with high diffusion resistance in copper metallization, J. Alloys Compd. 748 (2018) 258–264, https://doi.org/10.1016/j.jallcom.2018.03.084.

[34] R. Li, M. Li, C. Jiang, B. Qiao, W. Zhang, J. Xu, Thermal stability of AlCrTaTiZrMo-nitride high entropy film as a diffusion barrier for Cu metallization, J. Alloys Compd. 773 (2019) 482–489, https://doi.org/10.1016/j.jallcom.2018.09.283.

[35] R. Hollerweger, H. Riedl, M. Arndt, S. Kolozsvari, S. Primig, P.H. Mayrhofer, Guidelines for increasing the oxidation resistance of Ti-Al-N based coatings, Thin Solid Films 688 (May) (2019) 137290, https://doi.org/10.1016/j.tsf.2019.05.009.

[36] H. Asanuma, P. Polcik, S. Kolozsvari, F.F. Klimashin, H. Riedl, P.H. Mayrhofer, Cerium doping of Ti-Al-N coatings for excellent thermal stability and oxidation resistance, Surf. Coat. Technol. 326 (2017) 165–172, https://doi.org/10.1016/j.surfcoat.2017.07.037.

[37] M. Pfeiler, C. Scheu, H. Hutter, J. Schnöller, C. Michotte, C. Mitterer, M. Kathrein, On the effect of Ta on improved oxidation resistance of Ti–Al–Ta–N coatings, J. Vac. Sci. Technol. A 27 (3) (2009) 554–560, https://doi.org/10.1116/1.3119671.

[38] P. Ström, P. Petersson, M. Rubel, G. Possnert, A combined segmented anode gas ionization chamber and time-of-flight detector for heavy ion elastic recoil detection analysis, Rev. Sci. Instrum. 87 (10) (2016), https://doi.org/10.1063/1.4963709.

[39] M.V. Moro, R. Holeňák, L. Zendejas Medina, U. Jansson, D. Primetzhofer, Accurate high-resolution depth profiling of magnetron sputtered transition metal alloy films containing light species: a multi-method approach, Thin Solid Films 686 (July) (2019), https://doi.org/10.1016/j.tsf.2019.137416.

[40] H.Y. Qu, D. Primetzhofer, M.A. Arvizu, Z. Qiu, U. Cindemir, C.G. Granqvist, G. A. Niklasson, Electrochemical rejuvenation of anodically coloring electrochromic nickel oxide thin films, ACS Appl. Mater. Interfaces 9 (49) (2017) 42420–42424, https://doi.org/10.1021/acsami.7b13815.

[41] W. Oliver, G. Pharr, An improved technique for determining hardness and elastic modulus using load and displacement sensing indentation experiments, J. Mater. Res. 7 (6) (1992) 1564–1583, https://doi.org/10.1557/jmr.1992.1564.

[42] G. Kresse, J. Furthmüller, Efficient iterative schemes for ab initio total-energy calculations using a plane-wave basis set, Phys. Rev. B Condens. Matter Mater. Phys. 54 (16) (1996) 11169–11186, https://doi.org/10.1103/PhysRevB.54.11169.

[43] G. Kresse, D. Joubert, From ultrasoft pseudopotentials to the projector augmented-wave method, Phys. Rev. B 59 (3) (1999) 1758–1775, https://doi.org/10.1103/PhysRevB.59.1758.

[44] W. Kohn, L.J. Sham, Self-consistent equations including exchange and correlation effects, Phys. Rev. 140 (4A) (1965) A1133–A1138, https://doi.org/10.1103/PhysRev.140.A1133.

[45] J.D. Pack, H.J. Monkhorst, Special points for Brillouin-zone integrations, Phys. Rev. B 16 (4) (1977) 1748–1749, https://doi.org/10.1103/PhysRevB.16.1748.

[46] S.H. Wei, L.G. Ferreira, J.E. Bernard, A. Zunger, Electronic properties of random alloys: special quasirandom structures, Phys. Rev. B 42 (15) (1990) 9622–9649, https://doi.org/10.1103/PhysRevB.42.9622.

[47] N. Koutná, D. Holec, O. Svoboda, F. F. Klimashin, P. H. Mayrhofer, Point defects stabilise cubic Mo-N and Ta-N, Journal of Physics D: Applied Physics 49 (37) (2016). arXiv:1604.02718, doi:https://doi.org/10.1088/0022-3727/49/37/375303.

[48] J. Patscheider, T. Zehnder, M. Diserens, Structure-performance relations in nanocomposite coatings, Surf. Coat. Technol. 146-147 (2001) 201–208, https://doi.org/10.1016/S0257-8972(01)01389-5.

[49] S. Vepřek, S. Reiprich, A concept for the design of novel superhard coatings, Thin Solid Films 268 (1–2) (1995) 64–71, https://doi.org/10.1016/0040-6090(95)06695-0.

[50] W. Ernst, J. Neidhardt, H. Willmann, B. Sartory, P.H. Mayrhofer, C. Mitterer, Thermal decomposition routes of CrN hard coatings synthesized by reactive arc evaporation and magnetron sputtering, Thin Solid Films 517 (2) (2008) 568–574, https://doi.org/10.1016/j.tsf.2008.06.086.

[51] C.M. Koller, A. Kirnbauer, R. Rachbauer, S. Kolozsvári, P.H. Mayrhofer, Thermally-induced phase transformation sequence of arc evaporated Ta-Al-N coatings, Scr. Mater. 113 (2016) 75–78, https://doi.org/10.1016/j.scriptamat.2015.09.040.

[52] L. Hultman, J. Bareño, A. Flink, H. Söderberg, K. Larsson, V. Petrova, M. Odén, J. E. Greene, I. Petrov, Interface structure in superhard TiN-SiN nanolaminates and nanocomposites: film growth experiments and ab initio calculations, Phys. Rev. B Condens. Matter Mater. Phys. 75 (15) (2007) 1–6, https://doi.org/10.1103/PhysRevB.75.155437.

[53] P.H. Mayrhofer, C. Mitterer, J.G. Wen, I. Petrov, J.E. Greene, Thermally induced self-hardening of nanocrystalline Ti-B-N thin films, J. Appl. Phys. 100 (4) (2006), https://doi.org/10.1063/1.2222406.

[54] R. Riedel, M. Seher, Crystallization behaviour of amorphous silicon nitride, J. Eur. Ceram. Soc. 7 (1) (1991) 21–25, https://doi.org/10.1016/0955-2219(91)90049-6.

[55] A. Leyland, A. Matthews, On the significance of the H/E ratio in wear control: a nanocomposite coating approach to optimised tribological behaviour, Wear 246 (1–2) (2000) 1–11, https://doi.org/10.1016/S0043-1648(00)00488-9.

[56] R. Hahn, A. Kirnbauer, M. Bartosik, S. Kolozsvári, P.H. Mayrhofer, Toughness of Si alloyed high-entropy nitride coatings, Mater. Lett. 251 (2019) 238–240, https://doi.org/10.1016/j.matlet.2019.05.074.

[57] G. Tammann, Über Anlauffarben von Metallen, Z. Anorg. Allg. Chem. 111 (1) (1920) 78–89, https://doi.org/10.1002/zaac.19201110107.

[58] G. Tammann, W. Köster, Metallographische Mitteilungen aus dem Institut für physikalische Chemie der Universität Göttingen. CV. Die Geschwindigkeit der Einwirkung von Sauerstoff, Schwefelwasserstoff und Halogenen auf Metalle, Zeitschrift für anorganische und allgemeine, Chemie 123 (1) (1922) 196–224, https://doi.org/10.1002/zaac.19221230115.

[59] R. Rachbauer, D. Holec, P.H. Mayrhofer, Increased thermal stability of Ti-Al-N thin films by Ta alloying, Surf. Coat. Technol. 211 (2012) 98–103, https://doi.org/10.1016/j.surfcoat.2011.07.009.